

# Novel metrics and application of nearest-neighbor feature selection for comparing resting-state fMRI brain atlases

Bryan A. Dawkins<sup>1</sup>, Rayus Kuplicki<sup>2</sup>, Trang T. Le<sup>3</sup>, Alejandro A. Hernandez<sup>1</sup>,  
and Brett A. McKinney<sup>1,4,\*</sup>

<sup>1</sup>Department of Mathematics, University of Tulsa, Tulsa, OK 74104, USA

<sup>2</sup>Laureate Institute for Brain Research, Tulsa, OK 74136, USA

<sup>3</sup>Department of Biostatistics, Epidemiology and Informatics, University of  
Pennsylvania, Philadelphia, PA 19104

<sup>4</sup>Tandy School of Computer Science, University of Tulsa, Tulsa, OK 74104, USA

\*Correspondence: brett.mckinney@gmail.com

## Abstract

Resting-state functional connectivity MRI (rs-fMRI) data consists of correlation matrices, where correlations are computed between the time series from brain Regions of Interest (ROIs). There are many different parcellations of the human brain into collections of ROIs. These parcellations, or atlases, can be used in case-control studies in order to understand and accurately classify subject phenotypes. We present new metrics for nearest-neighbor distance-based feature selection at the ROI level. Using our new metrics, we apply a novel nearest-neighbor feature selection algorithm to calculate relative importance of ROIs for classification of a binary outcome including major depression and healthy controls in two existing brain atlases. We use integer programming to derive a mapping between brain atlases to determine spatially similar ROIs. With ROI importance scores and spatial similarity between atlases, we present a novel modality for the comparison of brain atlases and the selection of ROIs relevant to major depression.

## 1 Background

Resting-state fMRI data exists in high dimensions and has many sources of noise, such as physiological or motion related [1]. Feature selection is typically done with the purpose of determining brain regions of interest (ROIs) that accurately discriminate between cases and controls in order to understand a particular phenotype. The data consists of pairwise ROI-ROI correlations, where each ROI is a time series measuring brain activity in a particular region or regions of the brain while a subject is not performing a task. A typical data set consists of  $m$  subject-specific correlation matrices of dimension  $p \times p$ , where the pairwise correlations are computed between  $p$  ROI time series with respect to a particular brain atlas.

Nearest-neighbor distance-based feature selection in rs-fMRI data has been performed using the private evaporative cooling method, which used pairwise ROI-ROI correlations as predictors of a particular phenotype [2]. However, nearest-neighbor feature selection algorithms have not been applied at the ROI level to assess the relative importance of ROIs for a given phenotype. To address this, we have previously proposed a new distance metric that allows us to compute the importance of individual ROIs using a nearest-neighbor distance-based approach (cite theoretical paper). We use this new distance metric with a novel nearest-neighbor feature selection algorithm called Nearest-neighbor Projected Distance Regression (NPDR) in order to compute ROI importance and the corresponding pseudo P values [3]. Our analysis is done on subject rs-fMRI correlation

matrices generated by two well known brain atlases with spherical [4] and anatomically shaped [5] ROIs, to which we refer as Power and Shen atlases, respectively. Cross sections through each atlas were visualized (Fig. 1) using the Analysis of Functional NeuroImages (AFNI) software [6].

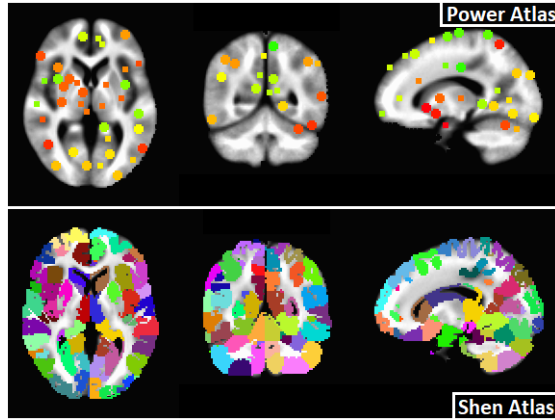


**Fig 1.** Two-dimensional slices through Power [4] and Shen [5] atlas ROIs. Slices are shown at the same locations in each atlas for the three different orientations. Atlases are in MNI space [7] so that voxel and ROI locations are comparable between them. Each atlas is labeled by the first author of the manuscripts in which they were introduced [4, 5].

In order to make spatial comparisons between any pair of brain atlases, we first compute a distance matrix containing all pairwise distances between the different collections of atlas ROIs. Distances are defined based on a set dissimilarity metric that accounts for differences in voxel collections between pairs of ROIs. In a particular coordinate system, voxels have well defined three-dimensional locations in a given brain atlas. As long as two different atlases are in the same coordinate system, we can compare voxel membership between opposing atlas ROIs. We use an integer program that defines the standard Assignment Problem (AP) to find the one-to-one mapping between the two sets of atlas ROIs [8]. The collection of all mapped ROIs gives the closest spatial analogy between the two atlases, which tells us the closest relationship between the two sets of ROIs from different atlases. The collection of unmapped ROIs gives an indication of spatial uniqueness in the two atlases, respectively. All ROIs can be further mapped to a well defined anatomical region of the brain, which allows us to point out potential targets for better understanding the phenotype of interest.

Our spatial mapping between atlases and relative importance scores for ROIs in each respective atlas provides a way to combine relevant and distinct aspects of each brain atlas into a new parcellation. This new atlas includes important ROIs that are in the optimal one-to-one mapping from the solution to the assignment problem and any important unmapped ROIs from each atlas. Spatial overlap and attribute importance can serve as a useful tool for other researchers to compare, contrast, and combine two atlases. In particular, our results show how one might choose either of the two atlases to study the phenotype of interest we are considering in this work.

## 2 Methods

In this section, we first describe real rs-fMRI data generated from healthy controls (HC) and subjects with major depressive disorder (MDD), eating disorder (ED), substance abuse (SA), or anxiety disorder (AD). Using integer programming, we then derive a one-to-one mapping between the ROIs in two brain atlases used to generate the real data mentioned previously. Finally, we use our new distance metric for rs-fMRI data, along with NPDR, to compute importance scores for ROIs in each atlas from the real data.

## 2.1 Real rs-fMRI data

This is where we describe the LIBR data.

## 2.2 Spatial overlap between brain atlases

Let  $R_A$  and  $R_B$  represent regions of interest (ROIs) in atlases  $A$  and  $B$ , respectively. We assume that atlases  $A$  and  $B$  are in the same coordinate space. Since  $R_A$  and  $R_B$  are just collections of voxels that have well defined three-dimensional coordinates within an atlas, the spatial overlap between  $R_A$  and  $R_B$  can be defined as the set intersection between the two ROIs. Spatial dissimilarity between  $R_A$  and  $R_B$  can be computed with the Jaccard metric, which is given by the following

$$d^J(R_A, R_B) = \frac{|R_A \cup R_B - R_A \cap R_B|}{|R_A \cup R_B|}, \quad (1)$$

where the  $(-)$  sign denotes set complement and  $|\cdot|$  represents set cardinality. If the intersection  $R_A \cap R_B$  is empty, then the two ROIs do not share any voxels and the Jaccard distance (Eq. 1) between them is 1. On the other hand, the Jaccard distance is 0 if the union  $R_A \cup R_B$  and intersection  $R_A \cap R_B$  are the same sets, which means the two ROIs have exactly the same voxels. All other possible Jaccard distances between  $R_A$  and  $R_B$  are strictly within  $(0, 1)$ . Hence, the Jaccard metric is contained within  $[0, 1]$ . The reason for division by  $|R_A \cup R_B|$  in the denominator of the Jaccard metric (Eq. 1) is specifically to normalized the distance to be within  $[0, 1]$ . Otherwise, this distance between two ROIs would be affected by the cardinalities of  $R_A$  and  $R_B$ , respectively. The Jaccard metric is intuitive in this context because ROIs are not just points in space, but rather they can have irregular three-dimensional shapes. Therefore, a Euclidean metric that gives the straight-line distance between two points does not necessarily indicate ‘closeness’ between two ROIs. It is possible to compute the Euclidean distance between the centroids of two ROIs, but the ROIs may not share many voxels due to their potentially irregular shapes. Therefore, it is more informative to use a distance metric that uses set operations like the Jaccard metric (Eq. 1). We show an example (Fig. 2) of the Jaccard distance between ROIs  $R_A$  and  $R_B$  that contain  $n_1$  and  $n_2$  voxels, respectively.

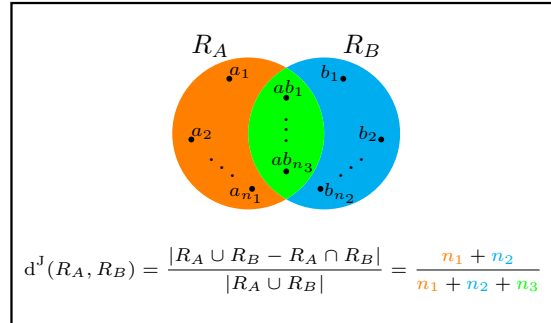


**Fig 2.** Example computation of Jaccard distance between ROIs  $R_A$  and  $R_B$  from two atlases  $A$  and  $B$ , respectively. There are  $n_1$ ,  $n_2$ ,  $n_3$  voxels in  $R_A$  only,  $R_B$  only, and both  $R_A$  and  $R_B$ , respectively. The numerator gives the number of voxels unique to  $R_A$  ( $n_1$ ) plus the number of voxels unique to  $R_B$  ( $n_2$ ). The denominator contains the total number of voxels in  $R_A$  or  $R_B$ .

Each ROI in atlas  $A$  may overlap many different ROIs in atlas  $B$ . On the other hand, some ROIs in  $A$  may not overlap any ROIs in  $B$ . Furthermore, it is likely that  $A$  and  $B$  contain different numbers of ROIs. If we want to compute a minimum distance one-to-one mapping between the atlases, it is possible that some ROIs in  $A$  will not have a mapped partner in  $B$ . In order to efficiently compute this atlas-atlas mapping, we formulate this task as a standard Assignment Problem [8], which has a very concise definition (Fig. 3).

$$\begin{array}{ll}
\text{Min} & \sum_{i=1}^M \sum_{j=1}^N d_{ij} y_{ij} \\
\text{s.t.} & \left. \begin{array}{l} \sum_{i=1}^M y_{i1} = 1 \\ \vdots \\ \sum_{i=1}^M y_{iN} = 1 \end{array} \right\} \text{Column Constraints} \\
& \left. \begin{array}{l} \sum_{j=1}^N y_{1j} = 1 \\ \vdots \\ \sum_{j=1}^N y_{Mj} = 1 \end{array} \right\} \text{Row Constraints} \\
& y_{ij} \in \{0, 1\} \quad \forall i, j
\end{array}$$

**Fig 3.** Assignment problem mathematical definition. The assignment matrix  $Y$  is binary, where  $y_{ij} = 0$  if nodes  $i$  and  $j$  are assigned to each other and 0 otherwise. The distance matrix  $D$  between all nodes is computed to assign costs to arcs (or edges) between nodes. The distance between nodes  $i$  and  $j$  is denoted by  $d_{ij}$ . Therefore, the objective function is the sum of all pairwise distances in the collection of assigned arcs. the column and row constraints dictate that each node is connected to exactly one and only one other node.

The objective function is the sum over all pairwise distances between nodes included in the mapping, where inclusion is determined by the binary solution matrix  $Y$  that has the following definition

$$y_{ij} = \begin{cases} 1 & \text{nodes } i \text{ and } j \text{ connected,} \\ 0 & \text{otherwise.} \end{cases} \quad (2)$$

Each row and each column of  $Y$  has a sum-to-one constraint, which means that each node in one collection is connected to exactly one other node in another disjoint collection. This problem assumes that the order (or size) of each collection is equal ( $M = N$  in Fig. 3), so that a one-to-one assignment is possible. In the context of brain atlases, we will satisfy this requirement by adding artificial variables to our solution matrix  $Y$ . Pairwise distances between actual ROIs in a brain atlas and an artificial variable will be given a large constant value, so that ROIs in atlas  $A$  will preferentially map to another ROI in  $B$  if a mapping is possible. Absent the possibility of a mapping, an ROI will map to an artificial variable, which implies that this particular ROI goes unmapped in our unconstrained solution. We show a diagram of atlas-atlas mapping (Fig. 4) that depicts ROIs as nodes and possible mappings as dashed lines between nodes in atlases  $A$  and  $B$ . Each possible mapping has a distance ( $d_{ij}$ ) associated with its inclusion in the solution matrix  $Y$ . The solution is ultimately found by choosing connections (solid lines) between atlas ROIs so that each ROI in  $A$  is connected to exactly one ROI in  $B$ , which simultaneously minimizes the sum of all distances in the mapping. We also show how this mapping might look with respect to the actual brain atlases we consider in this manuscript (Fig. 5). We have taken the unlabeled two-dimensional slices through each atlas (Fig. 1) and assigned ROIs to each other based on similar location. Each of the atlases are in the Montreal Neurological Institute (MNI) coordinate space [7], which allows us to compare the two atlases.

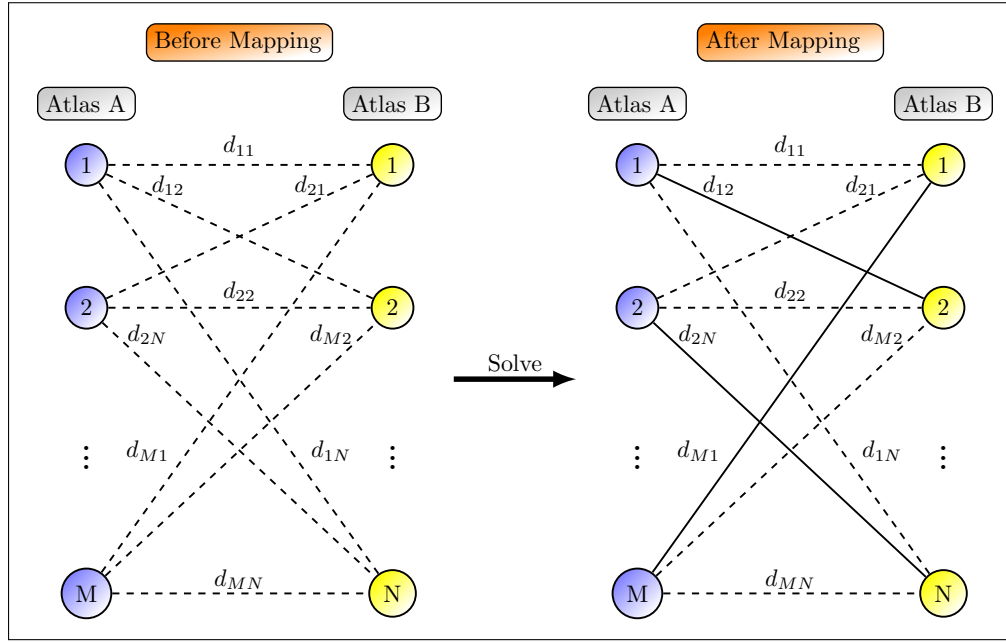


**Fig 4.** Assignment problem for brain atlas ROI-ROI mapping. Before the minimum distance pairwise mapping is found, all possible pairwise mappings are possible (dashed lines). Each ROI in atlas  $A$  must have exactly one partner in atlas  $B$ . After mapping, the minimum distance pairs are selected to give a one-to-one correspondence between ROIs (solid lines).

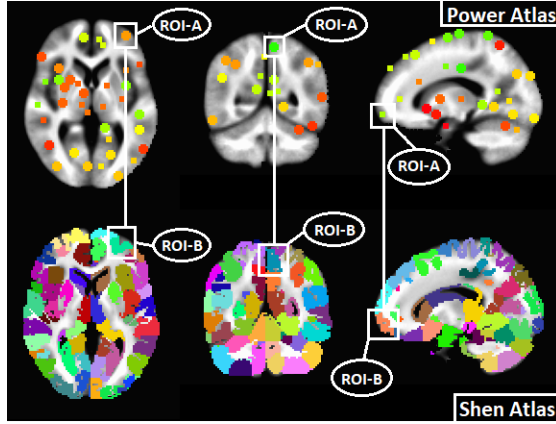


**Fig 5.** Visualization of mapping between Power and Shen atlas ROIs [4, 5]. ROIs that are in similar locations are potential partners in the resulting mapping from solving the assignment problem (Fig. 3). The Power atlas [4] is labeled atlas  $A$ , while the Shen atlas is labeled  $B$ .

### 2.3 Relative importance of ROIs

We load all subject-level resting-state fMRI (rs-fMRI) correlation matrices into a single matrix for our analysis (Fig. 6). Each column represents a single instance  $i \in \mathcal{I}$  and each consecutive collection of  $p - 1$  rows represents a single ROI  $a \in \mathcal{A}$ . We apply a Fisher r-to-z transform to all pairwise correlations and then standardize so that each column is approximately standard normally distributed ( $\mathcal{N}(0, 1)$ ).

$$\begin{array}{c}
\text{ROI}_1(a=1) \\
\text{ROI}_2(a=2) \\
\vdots \\
\text{ROI}_p(a=p)
\end{array}
\left\{
\begin{array}{c}
\begin{bmatrix}
\hat{A}_{12}^{(1)} & \hat{A}_{12}^{(2)} & \hat{A}_{12}^{(3)} & \cdots & \hat{A}_{12}^{(m)} \\
\hat{A}_{13}^{(1)} & \hat{A}_{13}^{(2)} & \hat{A}_{13}^{(3)} & \cdots & \hat{A}_{13}^{(m)} \\
\vdots & \vdots & \vdots & \cdots & \vdots \\
\hat{A}_{1p}^{(1)} & \hat{A}_{1p}^{(2)} & \hat{A}_{1p}^{(3)} & \cdots & \hat{A}_{1p}^{(m)}
\end{bmatrix} \\
\text{---} \\
\begin{bmatrix}
\hat{A}_{21}^{(1)} & \hat{A}_{21}^{(2)} & \hat{A}_{21}^{(3)} & \cdots & \hat{A}_{21}^{(m)} \\
\hat{A}_{23}^{(1)} & \hat{A}_{23}^{(2)} & \hat{A}_{23}^{(3)} & \cdots & \hat{A}_{23}^{(m)} \\
\vdots & \vdots & \vdots & \cdots & \vdots \\
\hat{A}_{2p}^{(1)} & \hat{A}_{2p}^{(2)} & \hat{A}_{2p}^{(3)} & \cdots & \hat{A}_{2p}^{(m)}
\end{bmatrix} \\
\text{---} \\
\begin{bmatrix}
\hat{A}_{p1}^{(1)} & \hat{A}_{p1}^{(2)} & \hat{A}_{p1}^{(3)} & \cdots & \hat{A}_{p1}^{(m)} \\
\hat{A}_{p2}^{(1)} & \hat{A}_{p2}^{(2)} & \hat{A}_{p2}^{(3)} & \cdots & \hat{A}_{p2}^{(m)} \\
\vdots & \vdots & \vdots & \cdots & \vdots \\
\hat{A}_{p,p-1}^{(1)} & \hat{A}_{p,p-1}^{(2)} & \hat{A}_{p,p-1}^{(3)} & \cdots & \hat{A}_{p,p-1}^{(m)}
\end{bmatrix}
\end{array}
\right\} = \mathbf{X}$$

**Fig 6.** Organization based on brain regions of interest (ROIs) of resting-state fMRI correlation dataset consisting of transformed correlation matrices for  $m$  subjects. Each column corresponds to an instance (or subject)  $I_j$  and each subset of rows corresponds to the correlations for an ROI attribute ( $p$  sets). The notation  $\hat{A}_{ak}^{(j)}$  represents the r-to-z transformed correlation between attributes (ROIs)  $a$  and  $k \neq a$  for instance  $j$ .

We determine attribute importance using Nearest-neighbor Projected Distance Regression (NPDR) [3], which is a novel nearest-neighbor feature selection method that builds upon Relief-Based Algorithms (RBAs) [9, 10]. For binary response variables, like case-control outcomes, NPDR computes a standardized beta coefficient for a generalized linear model (GLM) (Fig. 7). The argument to the logit function is  $p_{ij}^{\text{miss}}$ , which is the probability that instances  $i, j \in \mathcal{I}$  are in different phenotype classes. This argument models the binary outcome diff, which is given by the following

$$d_{ij}^{\text{miss}}(\vec{y}) = \begin{cases} 0 & y_i = y_j, \\ 1 & \text{else.} \end{cases} \quad (3)$$

For each coefficient  $\beta_a$ , a significant adjusted pseudo P value implies that the null hypothesis ( $\beta_a \leq 0$ ) is rejected. The alternative hypothesis ( $\beta_a > 0$ ) implies that the particular attribute  $a \in \mathcal{A}$  may be important for classification.

In order to compute distances, we previously introduced a metric for time series-correlation based (ts-corr) data like rs-fMRI (cite BoD theoretical). The one-dimensional projection (diff) onto a single ROI is define as follows

$$d_{ij}^{\text{ROI}}(a) = \sum_{k \neq a} |A_{ka}^{(i)} - A_{ka}^{(j)}|, \quad (4)$$

where  $A_{ak}^{(i)}$  and  $A_{ak}^{(j)}$  are the correlations between ROI  $a$  and ROI  $k$  for instances  $i, j \in \mathcal{I}$ , respectively. With this rs-fMRI diff, we define the pairwise distance between two instances  $i, j \in \mathcal{I}$  as follows

$$D_{ij}^{\text{fMRI}} = \sum_{a \in \mathcal{A}} d_{ij}^{\text{ROI}}(a). \quad (5)$$

Using our attribute diff (Eq. 4), we compute standardized beta coefficients of the generalized linear model given by

$$\text{logit}(p_{ij}^{\text{miss}}) = \beta_0 + \beta_a d_{ij}^{\text{ROI}}(a) + \epsilon_{ij}, \quad \forall (i, j) \in \mathcal{N}(k), \quad (6)$$

which is the GLM that NPDR uses to compute standardized beta coefficients for binary outcomes with  $d_{ij}(a)$  (Fig. 7) replaced by our diff for ROIs  $d_{ij}^{\text{ROI}}(a)$  (Eq. 4). The

collection of all neighbor ordered pairs is denoted by  $\mathcal{N}(k)$ . This set is a function of  $k$  because we use a fixed- $k$  approach in NPDR to allow each attribute  $a \in \mathcal{A}$  to have its own optimal value of  $k$ .

**Nearest-neighbor Projected Distance  
Regression (NPDR)**

For each  $a \in \mathcal{A}$  **do**

$$\text{logit} \left( p_{ij}^{\text{miss}} \right) = \beta_0 + \beta_a d_{ij}(a) + \epsilon_{ij}, \quad \forall (i, j) \in \mathcal{N}(k)$$

**Hypotheses**

$$\left. \begin{array}{l} H_0 : \beta_a \leq 0 \\ H_1 : \beta_a > 0 \end{array} \right\} p_{\text{adj}} < 0.05 \Rightarrow \text{reject } H_0$$

**Fig 7.** Nearest-neighbor Projected Distance Regression for binary response (case-control) [3]. For each attribute  $a \in \mathcal{A}$ , we compute standardized beta coefficients for a generalized linear model, where the predictors ( $d_{ij}(a) = |X_{ia} - X_{ja}|$ ) are one-dimensional projected distances (diffs) with respect to a particular attribute. The argument  $p_{ij}^{\text{miss}}$  is the probability that instances  $i, j \in \mathcal{I}$  are in different phenotype classes. The logit function models the binary hit-miss phenotype projection (Eq. 3). Significant adjusted pseudo P values ( $p_{\text{adj}}$ ) lead to the rejection of the null hypothesis  $\beta_a \leq 0$ . The set  $\mathcal{N}(k)$  is the collection of all neighbor ordered pairs such that each target instances neighborhood as exactly  $k$  nearest neighbors.

We employ an adaptive- $k$  algorithm called Gene-Wise Adaptive  $k$  (GWAK) that was originally developed for gene expression data [11] to determine the optimal  $k$  for each ROI in the two atlases we are analyzing. Although developed for gene expression data, this method can be used for other data types to which nearest-neighbor feature selection is applied. GWAK uses a greedy approach to optimize the relevance score for each attribute as a function of  $k$  (Fig. 8). For each attribute  $a \in \mathcal{A}$ , a relevance score is computed for each value of  $k = 1, 2, \dots, m - 1$  using some nearest-neighbor feature selection algorithm. Each attribute is assigned the value of  $k$  that maximizes its relevance score. For noise attributes, scores do not change significantly as a function of  $k$ . On the other hand, the scores of relevant attributes will change significantly as a function of  $k$ . This implies that GWAK maximizes the probability of detecting relevant attributes when nearest-neighbor feature selection is utilized.

We have previously shown that cross-validation approaches for tuning  $k$  to optimally select relevant features do not perform well in nearest-neighbor feature selection as compared to GWAK (cite simulation paper). This is due largely to the fact that cross-validation is optimizing test classification accuracy, which does not necessarily correlate with the relevance or quality of selected features. Partitioning data into training and test folds also limits the choice of  $k$  because the training data has only a subset of available instances in the full data set. This partitioning may cause the selection of a suboptimal  $k$  for a relevant attribute, which could be detrimental to the quality of selected features.

		Attributes				
		$a_1$	$a_2$	$a_3$	$\dots$	$a_p$
Neighbors ( $k$ )	1	-0.72	-0.98	0.85	$\dots$	-0.35
	2	0.67	0.60	-0.86	$\dots$	-0.12
	3	-0.52	0.83	0.12	$\dots$	0.61
	4	0.34	0.77	-0.42	$\dots$	0.84
	$\vdots$	$\vdots$	$\vdots$	$\vdots$	$\dots$	$\vdots$
	$m - 1$	0.11	-0.51	0.64	$\dots$	0.78
Winning Scores		0.67	0.83	0.85	$\dots$	0.84

**Fig 8.** Feature-wise adaptive- $k$  method for choosing optimal values of  $k$  in nearest-neighbor feature selection. For each attribute  $a \in \mathcal{A}$  and each value of  $k = 1, 2, \dots, m - 1$ , a score or weight is computed with a nearest-neighbor feature selection method like Relief-Based Algorithms (RBAs) or another similar method. Each feature is assigned the value of  $k$  that maximizes its importance score. Winning scores are then sorted in decreasing order and some fraction of the top scoring attributes are chosen for further analysis. We use the adjusted pseudo P values from NPDR to filter out attributes that are determined irrelevant to the phenotype. With NPDR, attribute scores are simply the standardized beta coefficients computed for the corresponding GLM (Eq. 6).

### 3 Results

In this section, we first give a pairwise mapping between the Power and Shen brain atlases. We describe the process of solving for a minimum distance one-to-one mapping. We then show which ROIs in the two atlases are determined important by NPDR, which are partitioned by those that are mapped and unmapped. Finally, we demonstrate the validity of important ROIs by referencing other analyses that have produced similar results.

#### 3.1 Power and Shen atlas mapping

Since there are 277 and 278 ROIs in Power and Shen atlases, respectively, we first compute a distance matrix  $D$  that contains all pairwise distances between atlas ROIs. This gives us a  $278 \times 277$  distance matrix to which we add a column of large numeric entries to represent distances from ROIs to an artificial variable. This makes the distance matrix square, which allows us to satisfy the one-to-one constraint of the Assignment Problem (Fig. 3). We used the open source statistical computing software **R** [12], which includes a package called **lpSolve** [13] for solving a variety of linear and integer programs. The **lpSolve** package contains a function `lp.assign()`, which simply takes a square distance matrix as input and produces solution matrix  $Y$  and an objective function value as output. For distance matrices comparable in dimension to  $D$ , the function elapses only a few seconds in run time.

The solution matrix from `lp.assign()` has a total of 230 actual mapped pairs. Some of the entries in the solution matrix  $Y$  are extraneous, which we define as one of the



following: an ROI pair including an artificial variable, an ROI pair for which the Jaccard dissimilarity is maximal (e.g.,  $d^J(R_A, R_B) = 1$ ), or an ROI pair for which the Jaccard dissimilarity is simply larger than another pairwise dissimilarity. Therefore, there are 47 and 48 unmapped ROIs from Power and Shen atlases, respectively. We give a summary of both mapped and unmapped ROIs from each atlas that includes the mapping assignment solution, corresponding brain region for each ROI, and corresponding functional network for each ROI (cite supplementary spreadsheets/tables). We also show a visualization of one atlas overlaid onto another (Fig. 9). Mapped ROIs from each atlas are highlighted to show relative spatial similarity (top of Fig. 9), which shows validation of the Assignment Problem solution. Unmapped ROIs from each atlas are highlighted to show relative spatial dissimilarity (bottom of Fig. 9), which similarly validates their categorization as extraneous mappings.

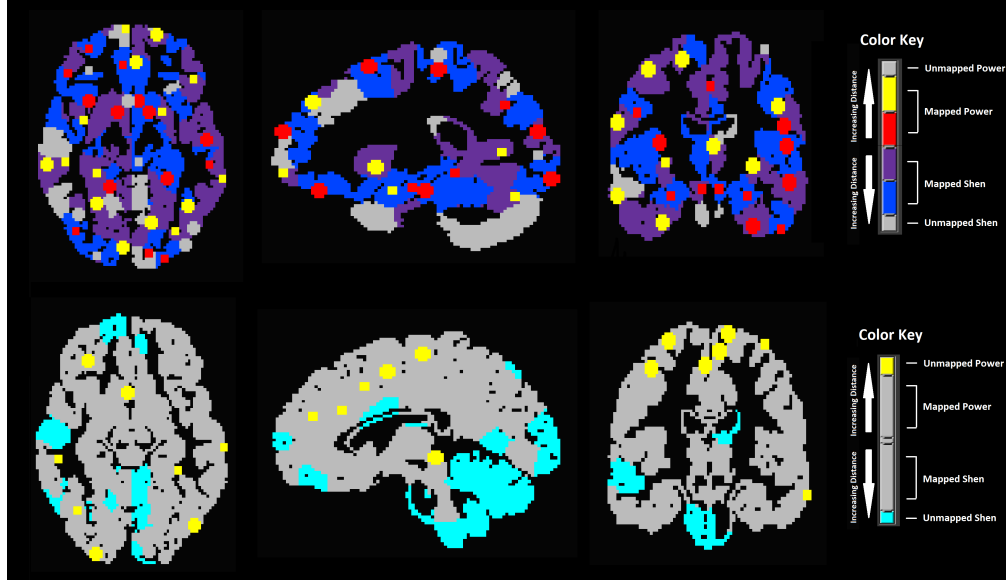


**Fig 9.** Visualization of mapped and unmapped ROIs from Power and Shen ROIs, respectively, from Assignment Problem solution. Two-dimensional slices from each atlas are overlaid on top of each other. The upper slices highlight the mapped ROIs from each atlas. The lower slices highlight the unmapped ROIs from each atlas.

Mapped ROIs are an indication of informational and spatial similarity shared by both atlases. Subject data that is derived from the mapped ROIs are highly correlated because each ROI pair shares voxels from which ROI time series are created. Unmapped ROIs in a single atlas may or may not intersect one of the mapped ROIs in another atlas. These unmapped ROIs indicate the most unique aspects of each atlas relative to one another. Hence, unmapped ROIs should be considered for inclusion in a customized atlas if determined to be important for predicting the outcome.

### 3.2 Power and Shen atlas ROIs relevant to MDD

We used GWAK to determine the value of  $k$  that maximized the NPDR standardized beta coefficient  $\beta_a$  (Eq. 6) for each atlas ROI. Important mapped (Table 1) and unmapped (Table 2) Power ROIs correspond to several brain regions with known associations with MDD. The highest ranked Power ROI is designated as 89 with respect to that atlas, which is in the right precuneus brain region in the dorsal default mode network (DMN). The precuneus in general, and the right precuneus in particular, has previously been associated with MDD [14–16].

Aside from the left middle temporal gyrus, each of the important mapped Power ROI brain regions (Table 1) has been identified in several other studies regarding MDD patients versus healthy controls: left inferior temporal gyrus [17,18], left parahippocampal gyrus [17,19], right middle frontal gyrus [20,21], left cingulate gyrus [22,23], right superior frontal gyrus [24,25], right supramarginal gyrus [26,27], right orbital gyrus [18,28], right medial frontal gyrus [24,29], right caudate head [30,31], right inferior frontal gyrus [24,27], right superior temporal gyrus [32], left lingual gyrus [33,34], and right cuneus [35,36].

Similar to the collection of important mapped Power ROIs (Table 1), each important unmapped Power ROI brain region, other than the left middle temporal gyrus, has been identified in other studies that compared MDD patients with healthy controls: right middle temporal gyrus [18], right inferior parietal lobule [37], left medial frontal gyrus [21], left insula [38,39], right postcentral gyrus [38], and left cingulate gyrus [22,23].

NPDR-detected functional networks relevant to MDD have all been previously associated with the disorder: dorsal default mode network (DMN) [15,40–44], left executive control network (LECN) [45–47], right executive control network (RECN) [45–47], language network [48,49], primary visual network [49], sensorimotor network [49–51], and anterior salience network [52,53].

Nearly every Shen atlas ROI intersects multiple brain regions, as determined by Shen ROI intersection with Power ROIs that have unique brain region associations. We highlighted brain regions corresponding to mapped and unmapped important Shen ROIs (Tables 3-4) that were not detected as important with respect to the Power atlas. Some of the highlighted brain regions for significant ROIs may not actually be relevant because many of the detected Shen ROIs intersect important Power ROIs. Some of the brain regions intersected by important Shen ROIs, such as left culmen, left declive, right lingual gyrus, locus coeruleus, right declive, right parahippocampal gyrus, left inferior frontal gyrus, right uvula, left superior temporal gyrus, left precentral gyrus, left inferior parietal lobule, right superior parietal lobule, left middle occipital gyrus, left inferior occipital gyrus, right paracentral lobule, and left middle frontal, are the only brain regions associated with the particular Shen ROI. Almost all of these regions are relevant to MDD, but more investigation must be done to determine if the corresponding Shen ROI is important due to the incorporation of these brain regions or if significance is related to another associated brain region. For example, the most significant Shen ROI is labeled 243 (Table 3), which intersects the left inferior temporal gyrus, the left parahippocampal gyrus, and the left fusiform gyrus. The left inferior temporal gyrus and left parahippocampal gyrus are the brain regions that contain ROIs 4 and 77 in the Power atlas (Table 1), which are among the top 3 significant Power ROIs. This confounds our ability to label the left fusiform gyrus as important with respect to these two atlases, however, this brain region has been associated with MDD in other studies [54,55].

Nearly all brain regions intersected by important Shen ROIs, but not containing any important Power ROIs, are all associated with MDD in other studies: left fusiform gyrus [54,55], right insula [56,57], right lentiform nucleus [58,59], left superior frontal gyrus [21,24], left culmen [60,61], left declive [60,62], right lingual gyrus [33,34], left postcentral gyrus [38,63], left precentral gyrus [64,65], right inferior occipital gyrus [66,67], locus coeruleus [68,69], right declive [60,62], right fusiform gyrus [55,70], right inferior temporal gyrus [17], right parahippocampal gyrus [71,72], left paracentral lobule [18,73], left inferior frontal gyrus [24,74], right uvula [75], left inferior occipital gyrus [67], left middle occipital gyrus [76,77], left superior temporal gyrus, left inferior parietal lobule, right superior parietal lobule, right paracentral lobule, right angular gyrus, left cuneus, left middle frontal gyrus, right precentral gyrus, left uncus, right middle occipital gyrus.

**Table 1.** Standardized beta coefficients, P values, and brain regions for important mapped Power atlas ROIs.

ROI	$\beta_a$	P Value	Brain Region	Func. Network
89	5.6464	5.87e-06	Right Precuneus	Dorsal DMN
4	5.3591	2.49e-05	Left Inferior Temporal Gyrus	LECN
77	5.1431	8.35e-05	Left Parahippocampal Gyrus	Dorsal DMN
181	4.7650	4.28e-04	Right Middle Frontal Gyrus	RECN
59	4.6523	7.55e-04	Left Cingulate Gyrus	Anterior Salience
180	4.6062	8.86e-04	Right Superior Frontal Gyrus	NA
204	4.5755	1.04e-03	Right Supramarginal Gyrus	RECN
5	4.5654	1.07e-03	Right Orbital Gyrus	Dorsal DMN
110	4.3227	3.08e-03	Right Medial Frontal Gyrus	Dorsal DMN
129	4.2442	4.23e-03	Left Middle Temporal Gyrus	Language
76	4.2390	4.60e-03	Right Medial Frontal Gyrus	Dorsal DMN
270	4.1885	5.29e-03	Right Caudate Head	NA
85	3.8958	1.72e-02	Right Inferior Frontal Gyrus	NA
82	3.8729	1.88e-02	Right Superior Temporal Gyrus	NA
160	3.7058	3.54e-02	Left Lingual Gyrus	Primary Visual
145	3.6940	3.76e-02	Right Cuneus	Primary Visual

**Table 2.** Standardized beta coefficients, P values, and brain regions for important unmapped Power atlas ROIs.

ROI	$\beta_a$	P Value	Brain Region	Func. Network
83	5.6804	4.92e-06	Left Middle Temporal Gyrus	LECN
128	4.9002	2.32e-04	Right Middle Temporal Gyrus	NA
192	4.0946	7.95e-03	Right Inferior Parietal Lobule	RECN
35	4.0692	8.59e-03	Left Medial Frontal Gyrus	Sensorimotor
73	4.0154	1.08e-02	Left Insula	NA
36	3.8673	2.19e-02	Right Postcentral Gyrus	Sensorimotor
213	3.6807	4.52e-02	Left Cingulate Gyrus	Anterior Salience

**Table 3.** Standardized beta coefficients, P values, and brain regions for important mapped Shen atlas ROIs. Brain regions were assigned to each Shen ROI based on overlap with known Power ROI brain regions. Brain regions for Shen ROIs that did not overlap any Power ROIs were assigned NA. Brain regions that did not show up in the list of important Power ROIs (Tables 1-2) are highlighted.

ROI	$\beta_a$	P Value	Brain Region
243	13.4157	2.41e-38	Left Inferior Temporal Gyrus, Left Parahippocampal Gyrus, Left Fusiform Gyrus
99	13.1216	1.09e-36	Right Middle Temporal Gyrus, Right Insula, Right Lenticular Nucleus
5	11.6413	7.29e-29	Right Postcentral Gyrus, Right Inferior Parietal Lobule
29	11.3464	2.06e-27	Right Postcentral Gyrus
277	9.5110	3.64e-19	Left Superior Frontal Gyrus, Left Medial Frontal Gyrus
178	9.1192	1.40e-17	Left Culmen, Left Declive

Continued on next page

Table 3 – continued from previous page

ROI	$\beta_a$	P Value	Brain Region
127	8.5795	1.66e-15	Right Lingual Gyrus
105	7.4976	1.03e-11	Right Medial Frontal Gyrus, Right Middle Frontal Gyrus, Right Superior Frontal Gyrus
262	7.4889	1.10e-11	Left Postcentral Gyrus, Left Precentral Gyrus, Left Medial Frontal Gyrus
96	7.0001	3.94e-10	Right Inferior Occipital Gyrus, Right Lingual Gyrus
239	6.9550	5.39e-10	Locus Coeruleus
104	6.8045	1.54e-09	Right Declive
217	6.6554	4.25e-09	Left Parahippocampal Gyrus, Left Fusiform Gyrus
238	6.4225	2.00e-08	Left Middle Temporal Gyrus
83	6.3879	2.55e-08	Right Superior Temporal Gyrus
57	6.3269	3.71e-08	Right Inferior Parietal Lobule, Right Postcentral Gyrus
7	6.2803	5.01e-08	Right Middle Frontal Gyrus, Right Precentral Gyrus
12	6.2222	7.29e-08	Right Lingual Gyrus, Right Cuneus
32	6.1985	8.42e-08	Right Precentral Gyrus, Right Postcentral Gyrus
102	6.1316	1.28e-07	Right Inferior Occipital Gyrus, Right Middle Occipital Gyrus
19	6.0343	2.34e-07	Right Fusiform Gyrus, Right Middle Temporal Gyrus, Right Inferior Temporal Gyrus
21	6.0037	2.83e-07	Right Cingulate Gyrus, Right Precuneus
202	5.7008	1.74e-06	Left Declive, Left Culmen
136	5.6781	1.98e-06	Right Parahippocampal Gyrus
253	5.5841	3.40e-06	Right Medial Frontal Gyrus, Left Medial Frontal Gyrus, Left Paracentral Lobule
113	5.4798	6.17e-06	Right Culmen, Right Parahippocampal Gyrus
271	5.3379	1.41e-05	Left Medial Frontal Gyrus
215	5.2170	2.86e-05	Left Inferior Frontal Gyrus
130	5.1917	2.99e-05	Right Uvula
257	5.0391	6.68e-05	Left Lingual Gyrus, Left Inferior Occipital Gyrus, Left Middle Occipital Gyrus
237	5.0153	7.61e-05	Left Superior Temporal Gyrus, Left Precentral Gyrus
245	5.0136	7.68e-05	Left Superior Temporal Gyrus, Left Inferior Parietal Lobule
80	4.7380	3.07e-04	Right Superior Parietal Lobule, Right Precuneus
247	4.7039	3.63e-04	Left Middle Occipital Gyrus, Left Inferior Occipital Gyrus
55	4.5641	7.10e-04	Right Paracentral Lobule, Left Cingulate Gyrus, Right Medial Frontal Gyrus
8	4.5240	8.59e-04	Right Postcentral Gyrus
45	4.4630	1.14e-03	Right Medial Frontal Gyrus, Right Postcentral Gyrus
24	4.4623	1.15e-03	Right Supramarginal Gyrus, Right Angular Gyrus, Right Inferior Parietal Lobule
84	4.4571	1.18e-03	Left Cuneus, Right Precuneus, Right Cuneus
121	4.3935	1.58e-03	Right Lingual Gyrus
206	4.1698	4.32e-03	Left Inferior Frontal Gyrus
38	4.1499	4.83e-03	Right Uvula
193	4.1029	5.74e-03	Left Middle Frontal Gyrus
28	4.0366	7.66e-03	Right Postcentral Gyrus, Right Precentral Gyrus

Continued on next page

**Table 3 – continued from previous page**

ROI	$\beta_a$	P Value	Brain Region
213	3.9603	1.05e-02	Left Uncus, Left Parahippocampal Gyrus
147	3.8788	1.48e-02	Left Middle Occipital Gyrus, Left Middle Temporal Gyrus
87	3.8019	2.01e-02	Right Fusiform Gyrus, Right Middle Temporal Gyrus, Right Middle Occipital Gyrus
218	3.6315	3.96e-02	Left Precentral Gyrus
103	3.5907	4.64e-02	Right Inferior Frontal Gyrus

**Table 4.** Standardized beta coefficients, P values, and brain regions for important unmapped Shen atlas ROIs. Brain regions were assigned to each Shen ROI based on overlap with known Power ROI brain regions. Brain regions for Shen ROIs that did not overlap any Power ROIs were assigned NA.

ROI	$\beta_a$	P Value	Brain Region
49	9.5173	3.40e-19	NA
3	9.3489	1.67e-18	Right Medial Frontal Gyrus
76	9.0332	3.04e-17	NA
79	9.0313	3.08e-17	NA
175	8.4150	6.68e-15	Right Declive
219	7.8334	7.68e-13	NA
35	7.7575	1.39e-12	Right Middle Temporal Gyrus
231	7.5458	7.13e-12	Left Declive, Right Declive, Left Lingual Gyrus
174	7.5352	7.72e-12	NA
256	7.3053	4.32e-11	Left Declive
141	7.2127	8.50e-11	NA
13	6.2918	4.65e-08	NA
158	6.2916	4.67e-08	NA
196	5.9340	4.33e-07	NA
126	4.9343	1.15e-04	Right Uvula
31	4.8789	1.52e-04	NA
70	4.8009	2.25e-04	NA
115	4.6691	4.33e-04	Locus Coeruleus

### 3.3 Validation of NPDR detected ROIs

NPDR successfully detects ROIs that have been associated with MDD in numerous other studies.

## 4 Discussion

## References

- César Caballero Gaudes and Richard C. Reynolds. Methods for cleaning the BOLD fMRI signal. *NeuroImage*, 154:128–149, December 2017.
- Trang T Le, W Kyle Simmons, Masaya Misaki, Jerzy Bodurka, Bill C White, Jonathan Savitz, and Brett A McKinney. Differential privacy-based evapora-

- tive cooling feature selection and classification with relief-f and random forests. *Bioinformatics*, 33(18):2906–2913, 2017. 283 284
3. Trang T. Le, Bryan A. Dawkins, and Brett A. McKinney. Nearest-neighbor Projected-Distance Regression (NPDR) detects network interactions and controls for confounding and multiple testing. *Under Review*, 2019. 285 286 287
  4. Jonathan D Power, Alexander L Cohen, Stephen M Nelson, Gagan S Wig, Kelly Anne Barnes, Jessica A Church, Alecia C Vogel, Timothy O Laumann, Fran M Miezin, Bradley L Schlaggar, and Steven E Peterson. Functional network organization of the human brain. *Neuron*, 72(4):665–678, November 2011. 288 289 290 291
  5. X. Shen, F. Tokoglu, X. Papademetris, and R. T. Constable. Groupwise whole-brain parcellation from resting-state fMRI data for network node identification. *Neuroimage*, (0):403–415, November 2013. 292 293 294
  6. RW Cox. AFNI: software for analysis and visualization of functional magnetic resonance neuroimages. *Computational Biomedical Research*, 29(3):162–173, June 1996. 295 296 297
  7. DL Collins, P Neelin, and TM Peters. Automatic 3D intersubject registration of MR volumetric data in standardized Talairach space. *Journal of Computer Assisted Tomography*, 18(2):192–205, April 1994. 298 299 300
  8. David W. Pentico. Assignment problems: A golden anniversary survey. *European Journal of Operational Research*, 176:774–793, November 2007. 301 302
  9. Marko Robnik Šikonja and Igor Kononenko. Theoretical and Empirical Analysis of ReliefF and RReliefF. *Machine Learning*, 53:23 – 69, February 2003. 303 304
  10. Ryan J. Urbanowicz, Randal S. Olson, Peter Schmitt, Melissa Meeker, and Jason H. Moore. Benchmarking relief-based feature selection methods for bioinformatics data mining. *Journal of Biomedical Informatics*, 85:168–188, 2018. 305 306 307
  11. Brett A McKinney, Bill C White, Diane E Grill, Peter W Li, Richard B Kennedy, Gregory A Poland, and Ann L Oberg. ReliefSeq: a gene-wise adaptive-K nearest-neighbor feature selection tool for finding gene-gene interactions and main effects in mRNA-Seq gene expression data. *PloS one*, 8(12):e81527, 2013. 308 309 310 311
  12. R Core Team. *R: A Language and Environment for Statistical Computing*. R Foundation for Statistical Computing, Vienna, Austria, 2017. 312 313
  13. Michel Berkelaar and others. *lpSolve: Interface to 'Lp\_solve' v. 5.5 to Solve Linear/Integer Programs*, 2015. R package version 5.6.13. 314 315
  14. Wei Cheng, Edmund T. Rolls, Jiang Qiu, Deyu Yang, Hongtao Ruan, Dongtao Wei, Libo Zhao, Jie Meng, Peng Xie, and Jianfeng Feng. Functional Connectivity of the Precuneus in Unmedicated Patients With Depression. *Biological Psychiatry: Cognitive Neuroscience and Neuroimaging*, 3:1040–1049, December 2018. 316 317 318 319
  15. Arpan Dutta, Shane McKie, Darragh Downey, Emma Thomas, Gabriella Juhasz, Danilo Arnone, Rebecca Elliot, Steve Williams, J. F. William Deakin, and Ian M. Anderson. Regional default mode network connectivity in major depressive disorder: modulation by acute intravenous citalopram. *Translational Psychiatry*, 9(116), 2019. 320 321 322 323 324

16. Liu CH, Ma X, Yuan Z, Song LP, Jing B, Lu Hy, Tang LR, Fan J, Walter M, Liu CZ, Wang L, and Wang CY. Decreased Resting-State Activity in the Precuneus Is Associated With Depressive Episodes in Recurrent Depression. *J Clin Psychiatry*, 78(4):372–382, April 2017.
17. Mahdi Ramezani, Ingrid Johnsrude, Abtin Rasouljan, Rachael Bosma, Ryan Tong, and Tom Hollenstein. Temporal-lobe morphology differs between healthy adolescents and those with early-onset of depression. *NeuroImage: Clinical*, 6:145–155, August 2014.
18. Edmund T. Rolls, Wei Cheng, and Matthieu Gilson et al. Effective Connectivity in Depression. *Biological Psychiatry: Cognitive Neuroscience and Neuroimaging*, 2017.
19. Ling-Li Zeng, Hui Shen, Li Liu, Lubin Wang, Baojuan Li, Peng Fang, Zongtan Zhou, Yaming Li, and Dewen Hu. Identifying major depression using whole-brain functional connectivity: a multivariate pattern analysis. *BRAIN: A JOURNAL OF NEUROLOGY*, 135:1498–1507, March 2012.
20. Stephanie Reynolds, Normand Carrey, Natalia Jaworska, Lisa Marie Langevin, Xiao-Ru Yang, and Frank P MacMaster. Cortical thickness in youth with major depressive disorder. *BMC Psychiatry*, 14(83), 2014.
21. Paul B. Fitzgerald, Angela R. Laird, Jerome Maller, and Zafiris J. Daskalakis. A Meta-Analytic Study of Changes in Brain Activation in Depression. *Hum Brain Mapp*, 29(6):683–695, June 2008.
22. Clement Hamani, Helen Mayberg, Scellig Stone, Adrian Laxton, Suzanne Haber, and Andres M. Lozano. The Subcallosal Cingulate Gyrus in the Context of Major Depression. *BIOL PSYCHIATRY*, 69:301–308, 2011.
23. ME McLaren, SM Szymkowicz, A O’Shea, AJ Woods, SD Anton, and VM Dotson. Dimensions of depressive symptoms and cingulate volumes in older adults. *Transl Psychiatry*, 6, April 2016.
24. H Tao, S Guo, T Ge, KM Kendrick, Z Xue, Z Liu, and J Feng. Depression uncouples brain hate circuit. *Molecular Psychiatry*, 18:101–111, October 2013.
25. Giacomo Salvatore, Allison C. Nugent, Herve Lemaitre, David A. Luckenbaugh, Ruth Tinsley, Dara M. Cannon, Alexander Neumeister, Carlos A. Zarate Jr., and Wayne C. Drevets. Prefrontal cortical abnormalities in currently depressed versus currently remitted patients with major depressive disorder. *Neuroimage*, 54(4):2643–2651, February 2011.
26. Daihui Peng, Feng Shi, Gang Li, Drew Fralick, Ting Shen, Meihui Qiu, Jun Liu, Kaida Jiang, Dinggang Shen, and Yiru Fang. Surface Vulnerability of Cerebral Cortex to Major Depressive Disorder. *PLoS ONE*, March 2015.
27. Zhe Tu, Yuan Yuan Jia, Tao Wang, Hang Qu, Jun Xi Pan, Jie Jie, Xiao Yan Xu, Hai Yang Wang, and Peng Xie. Modulatory interactions of resting-state brain functional connectivity in major depressive disorder. *Neuropsychiatric Disease and Treatment*, 14:2461–2472, 2018.
28. Rui Yan, ShiWan Tao, HaiYan Liu, Yu Chen, JiaBo Shi, YuYin Yang, RongXin Zhu, ZhiJian Yao, and Qing Lu. Abnormal Alterations of Regional Spontaneous Neuronal Activity in Inferior Frontal Orbital Gyrus and Corresponding Brain Circuit Alterations: A Resting-State fMRI Study in Somatic Depression. *Frontiers in Psychiatry*, 10(267), April 2019.

29. Cédric Lemogne, Guillaume le Bastard, Helen Mayberg, Emmanuelle Volle, Loretzu Bergouignan, Stéphane Lehericy, Jean-François Allilaire, and Philippe Fossati. In search of the depressive self: extended medial prefrontal network during self-referential processing in major depression. *SCAN*, 4:305–312, March 2009.
30. Diego A. Pizzagalli, Avram J. Holmes, Daniel G. Dillon, Elena L. Goetz, Jeffrey L. Birk, Ryan Bogdan, Darin D. Dougherty, Dan V. Iosifescu, Scott L. Rauch, and Maurizio Fava. Reduced Caudate and Nucleus Accumbens Response to Rewards in Unmedicated Subjects with Major Depressive Disorder. *Am J Psychiatry*, 166(6):702–710, June 2009.
31. Robyn Bluhm, Peter Williamson, Ruth Lanius, Jean Théberge, Maria Densmore, Robert Bartha, Richard Neufeld, and Elizabeth Osuch. Resting state default-mode network connectivity in early depression using a seed region-of-interest analysis: Decreased connectivity with caudate nucleus. *Psychiatry and Clinical Neuroscience*, 63:754–761, August 2009.
32. Lisa A. Pan, Lisa Ramos, AnnaMaria Segreti, David A. Brent, and Mary L. Phillips. Right superior temporal gyrus volume in adolescents with a history of suicide attempt. *The British Journal of Psychiatry*, 206:339–340, 2015.
33. JeYoung Jung, June Kang, Eunsoo Won, Kichun Nam, Min-Soo Lee, Woo Suk Tae, and Byung-Joo Ham. Impact of lingual gyrus volume on antidepressant response and neurocognitive functions in Major Depressive Disorder: A voxel-based morphometry study. *Journal of Affective Disorders*, 169:179–187, August 2014.
34. Baptiste Couvy Duchesne, Lachlan T. Strike, Greig I. de Zubicaray, Katie L. McMahon, Paul M. Thompson, Ian B. Hickie, Nicholas G. Martin, and Margaret J. Wright. Lingual Gyrus Surface Area Is Associated with Anxiety-Depression Severity in Young Adults: A Genetic Clustering Approach. *Disorders of the Nervous System*, 5(1), February 2018.
35. Tongjian Bai, Meidan Zu, Yang Chen, Wen Xie, Chunlan Cai, Qiang Wei, Gong-Jun Ji, Yanghua Tian, and Kai Wang. Decreased Connection Between Reward Systems and Paralimbic Cortex in Depressive Patients. *Frontiers in Neuroscience*, 12(462), July 2018.
36. Hao Guo, Chen Cheng, Xiaohua Cao, Jie Xiang, Junjie Chen, and Kerang Zhang. Resting-state functional connectivity abnormalities in first-onset unmedicated depression. *Neural Regen Res.*, 9(2), January 2014.
37. Rebecca E. Cooney, Jutta Joorman, Fanny Eugène, Emily L. Dennis, and Ian H. Gotlib. Neural correlates of rumination in depression. *Cognitive, Affective, & Behavioral Neuroscience*, 10(4):470–478, 2010.
38. L Schmaal et al. Cortical abnormalities in adults and adolescents with major depression based on brain scans from 20 cohorts worldwide in the ENIGMA Major Depressive Disorder Working Group. *Molecular Psychiatry*, 22:900–909, May 2017.
39. Wenbin Li, Ziqi Chen, Min Wu, Hongyan Zhu, Lei Gu, Youjin Zhao, Weihong Kuang, Feng Bi, Graham J. Kemp, and Qiyong Gong. Characterization of brain blood flow and the amplitude of low-frequency fluctuations in major depressive disorder: A multimodal meta-analysis. *Journal of Affective Disorders*, 210:303–311, December 2017.



40. J. Paul Hamilton, Madison Farmer, Phoebe Fogelman, and Ian H. Gotlib. Depressive Rumination, the Default-Mode Network, and the Dark Matter of Clinical Neuroscience. *Biol Psychiatry*, 78(4):224–230, August 2015.
41. Chao-Gan Yan et al. Reduced default mode network functional connectivity in patients with recurrent major depressive disorder. *PNAS*, 116(18):9078–9083, April 2019.
42. Giannis Lois and Michéle Wessa. Differential association of default mode network connectivity and rumination in healthy individuals and remitted MDD patients. *Social Cognitive and Affective Neuroscience*, pages 1792–1801, July 2016.
43. Wenbin Guo, Feng Liu, Jian Zhang, Zhikun Zhang, Liuyu Yu, Jianrong Liu, Huaifu Chen, and Changqing Xiao. Abnormal Default-Mode Network Homogeneity in First-Episode, Drug-Naive Major Depressive Disorder. *PLoS ONE*, 9(3), March 2014.
44. Vinod Menon. Large-scale brain networks and psychopathology: a unifying triple network model. *Trends in Cognitive Sciences*, 2011.
45. Qinghua Zhao, Zarnawab N. K. Swati, Hichem Metmer, Xiaoshuang Sang, and Jianfeng Lu. Investigating executive control network and default mode network dysfunction in major depressive disorder. *Neuroscience Letters*, 701, March 2019.
46. Kristen K. Ellard, Jared P. Zimmerman, Navneet Kaur, Koene R. A. Van Dijk, Joshua L. Roffman, Andrew A. Nierenberg, Darin D. Dougherty, Thilo Deckersbach, and Joan A. Camprodon. Functional Connectivity Between Anterior Insula and Key Nodes of Frontoparietal Executive Control and Salience Networks Distinguish Bipolar Depression From Unipolar Depression and Healthy Control Subjects. *Biological Psychiatry: Cognitive Neuroscience and Neuroimaging*, 3:473–484, May 2018.
47. Li Liu, Ling-Li Zeng, Yaming Li, Qiongmin Ma, Baojuan Li, Hui Shen, and Dewen Hu. Altered Cerebellar Functional Connectivity with Intrinsic Connectivity Networks in Adults with Major Depressive Disorder. *PLoS ONE*, 7(6), June 2012.
48. Douglas H. Schultz, Takuya Lto, Levi I. Solomyak, Richard H. Chen, Ravi D. Mill, Alan Antecvic, and Michael W. Cole. Global connectivity of the frontoparietal cognitive control network is related to depression symptoms in the general population. *Network Neuroscience*, April 2018.
49. Xing-jie Wu, Ling-Li Zeng, Hui Shen, Lin Yuan, Jian Qin, Peng Zhang, and Dewen Hu. Functional network connectivity alterations in schizophrenia and depression. *Psychiatry Research: Neuroimaging*, 263:113–120, March 2017.
50. Dongmei Zhi, Vince D. Calhoun, Luxian Lv, Xiaohong Ma, Qing Ke, Zening Fu, Yuhui Du, Yongfeng Yang, Xiao Yang, Miao Pan, Shile Qi, Rongtao Jiang, Qingbao Yu, and Jing Sui. Aberrant Dynamic Functional Network Connectivity and Graph Properties in Major Depressive Disorder. *Frontiers in Psychiatry*, 9(339), July 2018.
51. Chuanjun Zhuo, Jiajia Zhu, Chunli Wang, Hongru Qu, Xiaolei Ma, and Wen Qin. Different spatial patterns of brain atrophy and global functional connectivity impairments in major depressive disorder. *Brain Imaging and Behavior*, 11:1678–1689, 2017.

52. Magdalena Sikora, Joseph Heffernan, Erich T. Avery, Brian J. Mickey, Jon-Kar Zubieta, and Marta Pecina. Salience Network Functional Connectivity Predicts Placebo Effects in Major Depression. *Biol Psychiatry Cogn Neurosci Neuroimaging*, 1(1), January 2017.
53. Xiang Wang, Dost Öngür, Randy P. Auerbach, and Shuqiao Yao. Cognitive Vulnerability to Major Depression: View from the Intrinsic Network and Cross-network Interactions. *Harvard Review of Psychiatry*, 24(3), June 2016.
54. Sarina J. Iwabuchi, Rajeev Krishnadas, Chunbo Li, Dorothee P. Auer, Joaquim Radua, and Lena Palaniyappan. Localized connectivity in depression: A meta-analysis of resting state functional imaging studies. *Neuroscience and Biobehavioral Reviews*, 51:77–86, January 2015.
55. Marijn C. W. Kroes, Michael D. Rugg, Matthew G. Whalley, and Chris R. Brewin. Structural brain abnormalities common to posttraumatic stress disorder and depression. *J Psychiatry Neurosci*, 36(4), October 2011.
56. Jason Avery, Wayne C. Drevets, Scott Moseman, Jerzy Bodurka, and W. Kyle Simmons. Major depressive disorder is associated with abnormal interoceptive activity and functional connectivity in the insula. *Biol Psychiatry*, 76(3):258–266, August 2014.
57. Sarina J. Iwabuchi, Daihui Peng, Yiru Fang Kaida Jiang, Elizabeth B Liddle, Peter F. Liddle, and Lena Palaniyappan. Alterations in effective connectivity anchored on the insula in major depressive disorder. *European Neuropsychopharmacology*, 24:1784–1792, August 2014.
58. Su Lui, Laura M. Parkes, Xiaoqi Huang, Ke Zou, Raymond C. K. Chan, Hong Yang, Ling Zou, Dongming Li, Hehan Tang, Tijiang Zhang, Xiuli Li, Yi Wei, Long Chen, Xueli Sun, Graham J. Kemp, and Qi-Yong Gong. Altered Cerebral Perfusion Measured with Arterial Spin-labeling MR Imaging. *Neuroradiology*, 251(2), May 2009.
59. Katharina Helm, Kathrin Viol, Thomas M Weiger, Peter A Tass, Christian Grefkes, Damir del Monte, and Günter Schiepek. Neuronal connectivity in major depressive disorder: a systematic review. *Neuropsychiatric Disease and Treatment*, 14:2715–2737, 2018.
60. Liang Su, Yiyun Cai, Yifeng Xu, Anirban Dutt, Shexun Shi, and Elvira Bramon. Cerebral metabolism in major depressive disorder: a voxel-based meta-analysis of positron emission tomography studies. *BMC Psychiatry*, 14(321), 2014.
61. T Yamamura, Y Okamoto, G Okada, Y Takaishi, M Takamura, A Mantani, A Kurata, Y Otagaki, H Yamashita, and S Yamawaki. Association of thalamic hyperactivity with treatment-resistant depression and poor response in early treatment for major depression: a resting-state fMRI study using fractional amplitude of low-frequency fluctuations. *Transl Psychiatry*, 6, March 2016.
62. Wei-Che Lin, Kun-Hsien Chou, Hsiu-Ling Chen, Chu-Chung Huang, Cheng-Hsien Lu, Shau-Hsuan Li, Ya-Ling Wang, Yu-Fan Cheng, Ching-Po Lin, and Chien-Chih Chen. Structural deficits in the emotion circuit and cerebellum are associated with depression, anxiety and cognitive dysfunction in methadone maintenance patients: A voxel-based morphometric study. *Psychiatry Research: Neuroimaging*, 201:89–97, May 2012.

63. Huifeng Zhang, Meihui Qiu, Lei Ding, David Mellor, Gang Li, Ting Shen, and Daihui Peng. Intrinsic gray-matter connectivity of the brain in major depressive disorder. *Journal of Affective Disorders*, 251:78–85, March 2019. 505 506 507
64. Noa Tsujii, Wakako Mikawa, Emi Tsujimoto, Toru Adachi, Atsushi Niwa, Hisae Ono, and Osamu Shirakawa. Reduced left precentral regional responses in patients with major depressive disorder and history of suicide attempts. *PLoS ONE*, April 2017. 508 509 510 511
65. Ting Shen, Cao Li, Biao Wang, Wei-min Yang, Chen Zhang, Zhiguo Wu, Mei-hui Qiu, Jun Liu, Yi-feng Xu, and Dai-hui Peng. Increased Cognition Connectivity Network in Major Depression Disorder: A fMRI Study. *Psychiatry Investig*, 12(2):227–234, February 2015. 512 513 514 515
66. Stuart M. Grieve, Mayuresh S. Korgaonkar, Stephen H. Koslow, Evian Gordon, and Leanne M. Williams. Widespread reductions in gray matter volume in depression. *NeuroImage: Clinical*, 3:332–339, September 2013. 516 517 518
67. Bradley S. Peterson, Virginia Warner, Ravi Bansal, Hongtu Zhu, Xuejun Hao, Jun Liu, Kathleen Durkin, Phillip B. Adams, Priya Wickramaratne, and Myrna M. Weissman. Cortical thinning in persons at increased familial risk for major depression. *PNAS*, 106(15):6273–6278, April 2009. 519 520 521 522
68. Bin Wang, Ying Wang, Qiong Wu, Hong-ping Huang, and Shao Li. Effects of  $\alpha$ 2A Adrenoreceptors on Norepinephrine Secretion from the Locus Coeruleus during Chronic Stress-Induced Depression. *Frontiers in Neuroscience*, May 2017. 523 524 525
69. Kenjiro Seki, Satomi Yoshida, and Manoj Kumar Jaiswal. Molecular mechanism of noradrenaline during the stress-induced major depressive disorder. *Neural Regeneration Research*, 13(7):1159–1169, October 2019. 526 527 528
70. Chen Lin, Yun Bian, Xiaole Han, Li Chen, Yu Zhu, and Dachun Chen. Gray Matter Reduction in Currently Depressed Patients of Major Depressive Disorder: A Meta-Analysis. *Neuropsychiatry (London)*, 7(5):596–605, 2017. 529 530 531
71. Vera Zamoscik, Silke Huffziger, Ulrich Ebner Premier, Christine Kuehner, and Peter Kirsch. Increased involvement of the parahippocampal gyri in a sad mood predicts future depressive symptoms. *SCAN*, 9:2034–2040, February 2014. 532 533 534
72. Navkiran Kalsi, Daniela Altavilla, Renata Tambelli, Paola Aceto, Cristina Trentini, Chiara Di Giorgio, and Carlo Lai. Neural Correlates of Outcome of the Psychotherapy Compared to Antidepressant Therapy in Anxiety and Depression Disorders: A Meta-Analysis. *Frontiers in Psychology*, 8(927), June 2017. 535 536 537 538
73. Preeti Sinha, R. Venkateswara Reddy, Purna Srivastava, and Urvakhsh M. Mehta. Network neurobiology of electroconvulsive therapy in patients with depression. *Psychiatry Research: Neuroimaging*, 287:31–40, March 2019. 539 540 541
74. Zhexue Xu, Jing Zhang, Di Wang, Ting Wang, Shu Zhang, Xi Ren, Xiaolei Zhu, Atsushi Kamiya, Jiliang Fang, and Miao Qu. Altered Brain Function in Drug-Naïve Major Depressive Disorder Patients With Early-Life Maltreatment: A Resting-State fMRI Study. *Frontiers in Psychiatry*, 10(255), April 2019. 542 543 544 545
75. Sophie R. DelDonno, Lisanne M. Jenkins, Natania A. Crane, Robin Nusslock, Kelly A. Ryan, Stewart A. Shankman, Luan Phan, and Scott A. Langenecker. Affective Traits and History of Depression Are Related to Ventral Striatum Connectivity. *J Affect Disord.*, 221:72–80, October 2018. 546 547 548 549

76. Xiaoyue Ma, Jia Liu, Taiyuan Liu, Lun Ma, Wenhui Wang, Shaojie Shi, Yan Wang, Qiyong Gong, and Meiyun Wang. Altered Resting-State Functional Activity in Medication-Naive Patients With First-Episode Major Depression Disorder vs. Healthy Control: A Quantitative Meta-Analysis. *Frontiers in Behavioral Neuroscience*, 13(89), May 2019.
77. Changjun Teng, Jing Zhou, Hui Ma, Yarong Tan, Xin Wu, Chengbin Guan, Huifen Qiao, Jijun Li, Yuan Zhong, Chun Wang, and Ning Zhang. Abnormal resting state activity of left middle occipital gyrus and its functional connectivity in female patients with major depressive disorder. *BMC Psychiatry*, 18(370), 2018.